Experimental Thermal and Fluid Science 140 (2023) 110758

Contents lists available at ScienceDirect

Experimental Thermal and Fluid Science

journal homepage: www.elsevier.com/locate/etfs

Effect of mass flow rate on bubble size distribution in boiling flow in temperature-controlled annular test section

Boštjan Zajec [a,b,*], Leon Cizelj [a], Boštjan Končar [a]

[a] Reactor Engineering Division, Jožef Stefan Institute, Jamova cesta 39, 1000 Ljubljana, Slovenia
[b] University of Ljubljana, Kongresni trg 12, 1000 Ljubljana, Slovenia

ARTICLE INFO

Keywords:
Flow boiling
Horizontal annulus
Flow visualization
Bubble size distribution
Heat flux measurement

ABSTRACT

Subcooled flow boiling experiments were performed in an annular horizontal channel with inner diameter of 12 mm and the gap of 2 mm. The annular channel is designed as a double-pipe heat exchanger, where the inner tube of the channel is heated by a water flow, providing a temperature-controlled boiling surface. The influence of mass flow rate of the working fluid R245fa on flow boiling patterns and heat transfer has been studied. Subcooled flow boiling patterns were recorded with a high-speed camera. The recorded images of the flow patterns were then further processed to determine the bubble size distributions, characterized as distributions of the void (vapour) volume given per bubble size. The observed bubble size distributions followed two distinct distribution functions: the Rayleigh distribution at larger and bimodal distribution at smaller mass flow rates. This indicates the existence of two distinct boiling flow regimes at different mass flow rates. The heat flux was estimated by local temperature measurements with thermocouples positioned along the boiling surface and in the heating water. The heat flux increased moderately with increasing mass flow rate, apparently without disruption at the observed change in the flow regime. On the contrary, the total void volume in the observed part of the test section is declining moderately with increased refrigerant mass flow rate, which, in this mode of operation of the test section, acts as a prevailing mechanism. The experimental setup, methods of experimental analysis and the results are presented and discussed.

1. Introduction

Boiling flow is an efficient heat transfer mechanism used in many systems, including air conditioning and refrigeration [1], power electronics [2] and large power systems such as thermal power plants and nuclear reactors [3]. Its wide utilization depends on many empirical correlations proposed for specific conditions including fluids, geometries, flow orientations, surface types and pressure [4–6]. The field thus receives a lot of attention, both from an experimental [7] and a numerical [8] point of view, however with a very limited success to derive a general and sufficiently accurate mechanistic model. At the lowest time and spatial scales, accurate numerical simulations of general two-phase flows are computationally very demanding [9] and moreover, still require some modelling by constitutive relations [10].

To successfully simulate boiling flow, a knowledge of basic bubble parameters is required. Bubbles change in size and shape as they move through the liquid, due to evaporation on the heated wall, condensation in the subcooled liquid core, and interactions with other bubbles. As these phenomena cannot be easily described by fundamental fluid mechanics equations, additional closure relations must be developed. All stages of bubble size evolution also require validation by experimental data. The size of the bubbles is reported in literature in many ways, including bubble departure diameters [11] and maximum bubble diameters [12]. It has also been studied through the variation of averaged bubble diameter due to different parameters [13].

Sugrue et al. [13] have studied the effects of various boiling parameters (incl. flow orientation) on the bubble departure diameter in subcooled flow boiling of deionized water in a square channel, and have proposed a new correlation for departure diameter [14]. Zeitoun et al. [15], investigated bubble behaviour in subcooled boiling of water in vertical annulus with inner tube outer diameter of $d_i = 12.7$ mm and gap size of $h_a = 6.3$ mm. They used high-speed imaging and image processing to determine the mean bubble diameter in the free flow, along with a single-beam gamma densitometer to determine the average void fraction. They proposed a correlation for mean Sauter diameter.

Traditionally, bubble diameters and void fractions were mainly re-

* Corresponding author at: Reactor Engineering Division, Jožef Stefan Institute, Jamova cesta 39, 1000 Ljubljana, Slovenia.
E-mail address: bostjan.zajec@ijs.si (B. Zajec).

https://doi.org/10.1016/j.expthermflusci.2022.110758
Received 24 July 2021; Received in revised form 26 April 2022; Accepted 14 August 2022
Available online 18 August 2022
0894-1777/

ported as integral or time-averaged values at certain locations [16–18]. Bottini et al. [17] performed local measurements of void fraction in flow boiling of water in vertical annulus ($d_i = 19.05$ mm, $h_a = 9.5$ mm) using four-point conductivity probes. Flow patterns were monitored with high-speed cameras at five different axial locations. They reported radial dependencies of void fractions and mean bubble diameters for two groups, separated by measured chord length. Chu et al. [16] have measured radial profiles of void fractions, mean Sauter diameter and bubble passing frequency in subcooled flow boiling of R134a in a pressurized vertical annulus ($d_i = 9.5$ mm, $h_a = 8.9$ mm). They have used high-speed camera for flow visualisation and optical fibres for void fraction measurement. Lee et al. [19] also studied subcooled boiling in vertical annulus ($d_i = 9.3$ mm, $h_a = 9.2$ mm) using water as a working fluid. They have measured radial profiles of local void fractions using a two-conductivity probe.

Recent advancements in high-speed cameras, data acquisition and imaging techniques also led to increased interest in bubble size distributions. They are especially important for the development of closure relations for modelling the vapour phase exchange between different bubble sizes in simulations using multigroup bubble models [20]. Originally bubble size was thought to follow normal distribution, but recent research shows that bubble size distributions mostly represent left-skewed distributions such as log-normal [20] and gamma distributions [21], while similarly-shaped Weibull distributions may also be appropriate [22]. Grau [23] also recently showed that distributions developed to model distributions of coal particles and droplet sizes, such as Rosin-Rammler [25] distribution and Nukiyama-Tanasawa distribution [24], are also distributions that have recently been shown to resemble on the bubble size distributions and can be used for this purpose.

Conde et al. [22] have recently measured the bubble size distributions in subcooled boiling in a horizontal square channel with a high-speed camera and image processing. They analysed different distributions, showed how bubble size distributions change with flow parameters, and proposed a new correlation for mean bubble diameter. They also presented a large database of bubble sizes for further post-processing. To the best of our knowledge, the work by Ugandhar et. al [26 27] is the only one describing the distribution of bubble sizes in a horizontal annulus. They have investigated the parametric effect of pressure on bubble size distributions in horizontal annulus ($d_i = 12.6$ mm, $h_a = 6.5$ mm) with boiling water as a working fluid. High-speed camera was used and automated image processing was applied in LabView IMAQ Vision building image processing software. All of the above-mentioned experiments used electric resistance heating of the boiling surface resulting in the heat flux control of the boiling process and flow patterns.

In the present work we rely for the first time on experiments performed within a horizontal annulus with temperature controlled boiling surface with inner tube outer diameter $d_i = 12$ mm and annular gap of $h_a = 2$ mm. Bubble size distributions, defined as relative contributions of different sizes of bubbles to the total void volume, were determined experimentally in the boiling flow of refrigerant R245fa. A high-speed camera with image processing was used to estimate the bubble size distributions in part of the test section. The key novelty of the present experiment is a water-heated test section, which provides a temperature-controlled heating for boiling flow experiments. Thus, the corresponding heat flux was determined from local temperature measurements by thermocouples positioned on the surface of the inner tube and in the heating water. The main focus of this study is to investigate the influence of the mass flow rate on the boiling flow patterns and heat flux in this type of test section.

2. Experimental setup

The utilized flow boiling experiment is part of the laboratory THELMA (Thermal Hydraulics experimental Laboratory for Multiphase Applications) at Reactor Engineering Division of Jožef Stefan Institute. When designing the laboratory, the widest possible range of test conditions was pursued. On the other hand, inherent constraints imposed by the given infrastructure, resources and the commitment to perform experiments at high accuracy levels needed to be considered. The design process and targeted accuracy values were described in detail by Matkovič et al. [28]. Chlorinated and fluorinated carbohydrate (CFC) refrigerants were selected for boiling fluids as they are easily accessible and widely used in both, industry and research. The requirement for temperature-controlled heat transfer determines another important design feature of the apparatus, the use of the heating fluid, which allows better control of the diabatic wall temperature. The experimental setup with the test section is shown in Fig. 1.

2.1. Experimental loop

The experimental setup contains several separate water loops and one closed refrigerant loop (Fig. 2), thermally connected to heat exchangers. Boiling takes place in the refrigerant loop. Refrigerant flows from the pump, through Coriolis mass flow meter and preheater, to the test section where it boils and then returns to the condenser. The condenser made from plate heat exchanger is sufficiently large that all vapour phase is fully condensed and only liquid enters the pump. Refrigerant R245fa is used for the present study as it enables boiling at low heat flux and low operating pressure, enabling operation at low heating powers of 1 kW or less. Special attention was given to supply a pure refrigerant, without oils commonly used in refrigeration technology.

Two adjacent water loops provide heating and cooling water for the heat exchangers and heating of the test section. Both water loops include large tanks (500 l and 800 l) with separate temperature control to ensure stable system temperatures. One tank provides water for heating of the test section, while the second one supplies the cooling water for the condenser. The mass flow rate of the heating water through the test section is measured by a Coriolis flow meter.

A temperature-controlled pressurizer, connected to the main refrigerant loop right after the pump, controls the overall system pressure. The pressurizer is a closed vessel containing a water-refrigerant heat exchanger to control the temperature. Heat exchanger made of copper pipes provides a large surface area on which refrigerant can boil or condense, keeping the mixture of vapour and liquid at saturated condition. Pressurizer is connected to the refrigerant loop after the gear pump at the lowest part of the experimental loop, and acts also as an expansion tank, which keeps the refrigerant level approximately constant. Temperature of the heating water in the pressuriser is controlled by Lauda thermal bath, representing a third separate water loop. Due to the refrigerant flow and associated pressure drop, the local pressure slightly varies along the piping in the system. Thus, at constant pressurizer settings, the inlet pressure on the test section also varies with the mass flow rate. The system is therefore partially pressure controlled. The average absolute pressure inside the system is controlled, but the inlet pressure on the test section is determined by the specific conditions of test section and condenser. The pressure at the test section inlet is measured by a pressure sensor. To setup a stable environment conditions, an air-conditioning unit maintains the air temperature in the lab constant (uncertainty of $\pm$ 1 °C) to ensure that heat losses on the test section and connecting pipes can be estimated.

2.2. Test section and instrumentation

The annular test section is the core of the experimental setup. It can be tilted to an arbitrary angle, from horizontal to vertical position. The horizontal layout has been used for the purpose of this study. A unique feature of this test section is its design, in principle representing a concentric tube heat exchanger (see Fig. 3) that enables a temperature-controlled heating of the working fluid [28]. Thus, unlike in power-

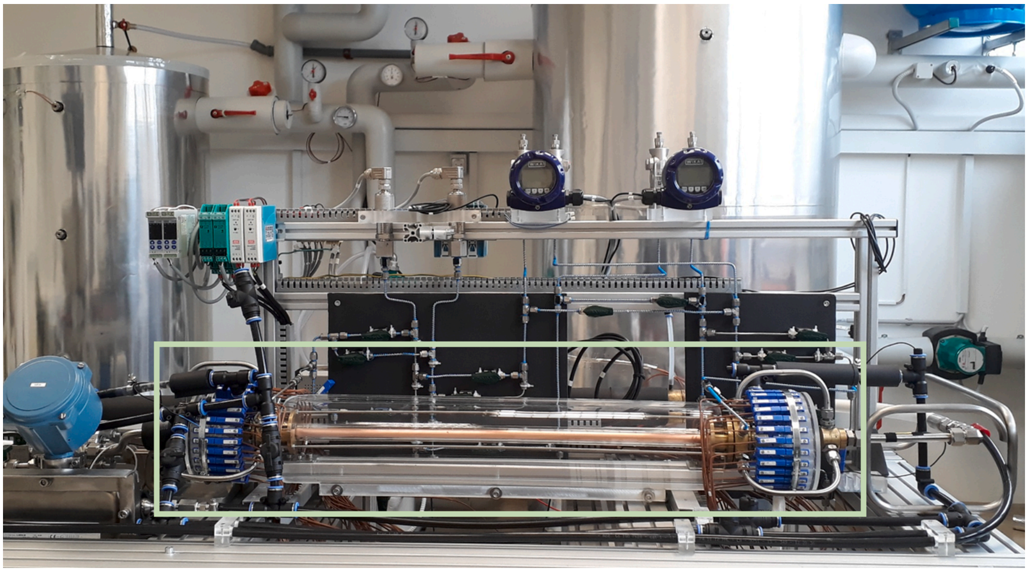

Fig. 1. Experimental setup with the test section. Test section is marked with a green frame. (For interpretation of the references to colour in this figure legend, the reader is referred to the web version of this article.)

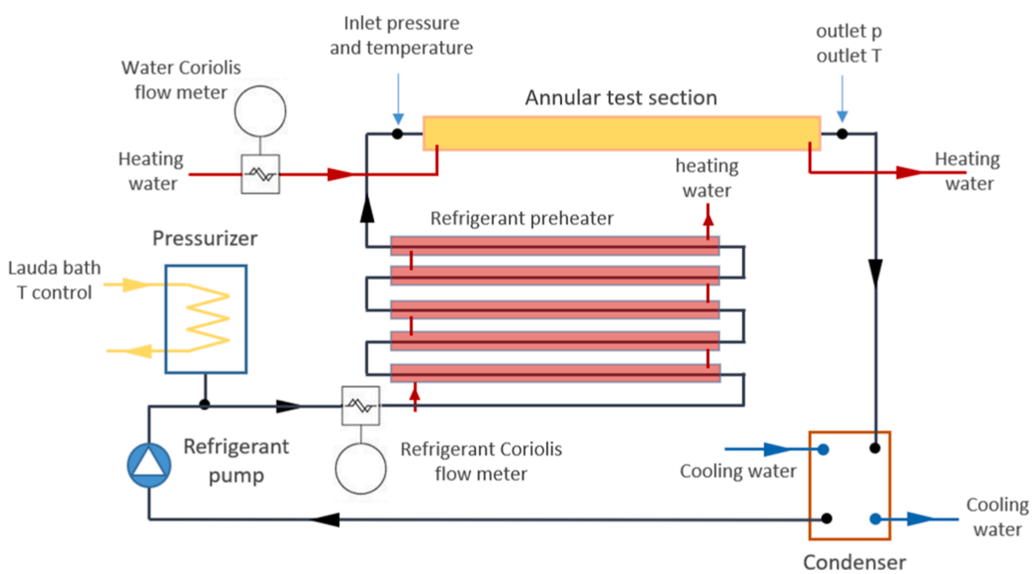

Fig. 2. Schematic of experimental loops. Refrigerant loop is shown in black. Heating and cooling water loops are shown in red and blue, respectively. (For interpretation of the references to colour in this figure legend, the reader is referred to the web version of this article.)

controlled heating, the operation near the critical heat flux condition is possible without the danger of overheating and burn out of the test section. This enables a wide range of measurements, from subcooled boiling to the critical heat flux and beyond into the unstable film-boiling regime. In such design, surface temperature and heat flux vary in axial direction and behave similarly as in the two-phase flow heat exchangers. Heat flux is not uniform and varies with the local temperature differences between the heating and boiling fluid. The local wall temperature and the heat flux variation in the test section are determined by measurements with thermocouples (denoted as TC in Fig. 3) positioned along the inner tube wall and in the heating water.

Boiling occurs at the outer surface of the inner copper tube with the outer diameter of 12 ± 0.1 mm and a total heated length of 585 ± 2 mm. The annular gap between the copper tube and the outer glass tube is 2 ± 0.1 mm. Outer surface of the copper tube was evenly brushed with 400-grit sand paper to provide a uniform distribution of nucleation sites. Boiling flow is observed through a 4 mm thick borosilicate glass tube and recorded with a high-speed camera.

Hot water flowing inside the copper tube transfers the heat to the refrigerant flowing in the annulus, which starts boiling at the tube outer surface at low temperatures (30 °C at 1.8 bar). Both, co-current and counter-current operation is possible in the test section. For measurements described in this paper, the co-current flow of heating water and refrigerant has been selected to achieve the maximum temperature difference between the water and the refrigerant in the inlet region. Specially designed finned structure inside of the copper tube provides strong heat transfer enhancement and allows local temperature measurement along the tube axis. Thermocouples for wall temperature measurements are installed in the fins just below the boiling surface, positioned in series, 21 ± 1 mm apart. To estimate the deviation of the surface temperatures from measured values, CFD simulations of the test section were performed [2930]. Thermocouples in contact with the heating water inside the channel measure the local temperature of water.

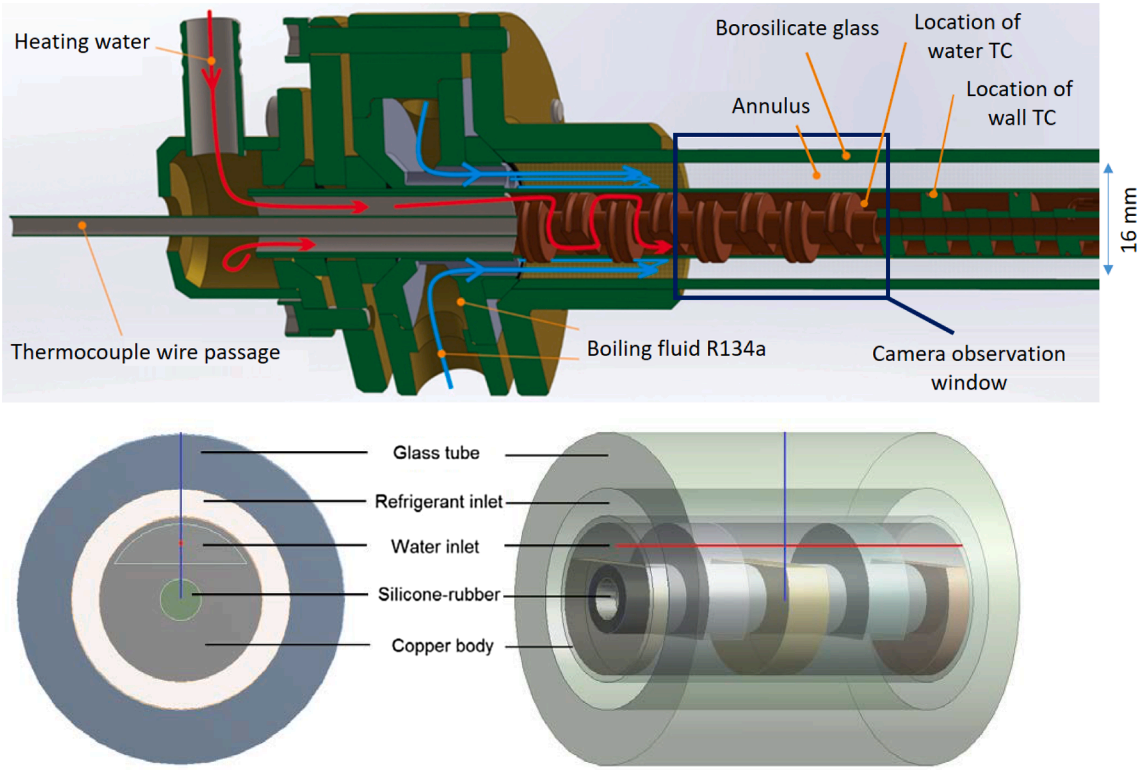

Fig. 3. Schematic of the test section with marked position of camera observation window. Top: inlet part of the test section, bottom: detail of the central part.

Two two-junction thermopiles are used to determine the temperature difference between the inlet and the outlet, as this gives higher accuracy than two separate thermocouples. Before inlet and outlet thermocouple locations, heating water is premixed by a spiral mixing element to ensure an accurate measurement. Two thermocouples at the water and refrigerant inlets are used to measure inlet temperature of the fluids and provide a reference temperature for the thermopiles. All thermocouples in the test section, including those at the inlet and outlet, are zero-referenced to the Kaye-170e artificial triple point of water. Air temperature is measured at two locations near the test section (2 and 5 cm away) with electronically referenced thermocouples.

In Table 1, the measurement accuracy of instrumentation used is listed. For inlet and outlet thermocouples, the absolute temperature uncertainty is stated. The thermocouples measuring the water temperature inside the test section were cross-calibrated at steady-state temperature conditions with water flow only. As they are used to determine the temperature gradient and only relative temperature difference is measured, their cross-calibration is sufficient to remove systematic errors (offsets between their values). The uncertainty of 0.1 °C can be adopted as a conservative value in this context. Measurement resolution is better as variations smaller than 0.1 °C are consistently observed with appropriate noise filtration and time averaging.

Table 1
Instrumentation and measurement uncertainties.

Measured quantity	Instrument	Nominal range	Uncertainty
Absolute pressure	WIKA membrane sensor	1–6 bar	± 0.1%
Pressure drop	WIKA membrane sensor	1–300 mbar	± 0.1%
Inlet temperatures	T-type thermocouple	10–70 °C	± 1 °C
Inlet/outlet T difference	Two-junction thermopile	0–100 °C	< 0.1 °C
Water temperatures / test-section	T-type thermocouple	10–70 °C	± 0.1 °C
Boiling surface temperatures	T-type thermocouple	10–70 °C	± 1 °C
Mass flow rate of water	Coriolis flow meter	0.01–300 kgh^{-1}	± 0.5%
Mass flow rate of R245fa	Coriolis flow meter	0.01–300 kgh^{-1}	± 0.5%

For absolute pressure measurement, two WIKA membrane pressure sensors are installed, one for lower pressure range, from 0 to 6 bar and one for higher range, from 0 to 25 bar. The lower range sensor is used for the considered experiments, while the high range sensor with lower accuracy is used as a control. Two WIKA differential pressure sensors have been applied to measure the pressure drop of the boiling refrigerant flow in the test section. All connecting tubes are electrically heated to prevent condensation and formation of bubbles that could influence the pressure readings. Two Micro Motion Emerson Coriolis flow meters are used for direct measurements of water and refrigerant mass flow rates. From these values, the mass flux (i.e. mass flow area density, kg s^{-1} m^{-2}) has been calculated, based on the cross-section area of the annulus. National Instruments PXIe 500 with LabVIEW software has been used for data acquisition.

2.3. *High-speed imaging setup*

For the visualization and recording of the flow, a Phantom 12-bit grayscale high-speed camera from LaVision PIV system is used with a 100 mm Macro 52.6 lens. This enables observation area of approx. 4.3 × 2.7 cm (1250 × 530 px). Due to geometrical constraints of the setup, camera is aligned out of the horizontal plane, as shown in Fig. 4.

In order to achieve a high depth of focus, the aperture of the camera needs to be closed as much as possible. However, as this reduces the amount of light hitting the sensor, a strong light source is needed. To supply a diffuse illumination from all directions, as well as minimizing reflections and shadows, a U-shaped lamp, built from high-power white LED strips, has been used. This results in a relatively even light distribution, except at the centre line, looking from the camera perspective

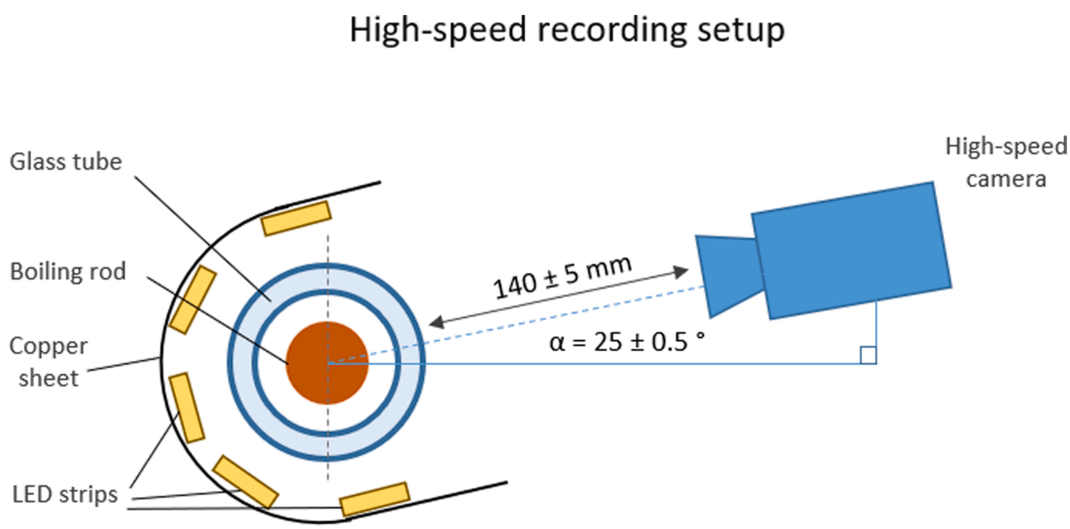

Fig. 4. High-speed camera and lighting configuration schematics (not to scale).

(shadow visible in Fig. 5). To reduce heating and its effects on the test section, the light only operated during image acquisition, after temperature measurements in the test section.

3. Data analysis

3.1. Heat flux measurement

Local heat flux in the test section is determined from temperatures measured by water thermocouples inside the inner tube. With the known mass flow rate of heating water Φ_m, the heat flux P between the two thermocouples can be calculated as.

$$P = \frac{\Phi_m c_p \Delta T}{A} = \frac{\Phi_m c_p}{2\pi \mathrm{r_a}} \frac{dT}{dx}, \tag{1}$$

where c_p is the specific heat of the water, ΔT is the temperature difference, A is the surface area between the two thermocouples and $\mathrm{r_a}$ is the radius of the copper tube. Due to the small observation window (see Fig. 3), only the first two thermocouples are in the visible frame of the camera. To reduce the uncertainty of the heat flux, first three water thermocouples at the beginning of the test section were used to fit the linear function and the resulting slope $\frac{dT}{dx}$ is used for calculation. Since the geometry is annular, all heat from internal water tube is transferred to the refrigerant. Axial heat conduction could be present, but its heat flux is several orders of magnitude smaller than the measured values and can therefore be neglected.

3.2. Determination of equivalent bubble sizes and bubble size distributions

Bubble size analysis was performed by analysing the high-speed recordings. Similarly, as in the work of Ugandhar et. al [26], the whole image was used for flow analysis. Several image pre-processing steps were performed to facilitate bubble identification and sizing, as shown in Fig. 5. To distinguish between the artefacts on the background and the bubbles, the image with blank background was first subtracted. The picture of the section filled solely with liquid phase without bubbles was

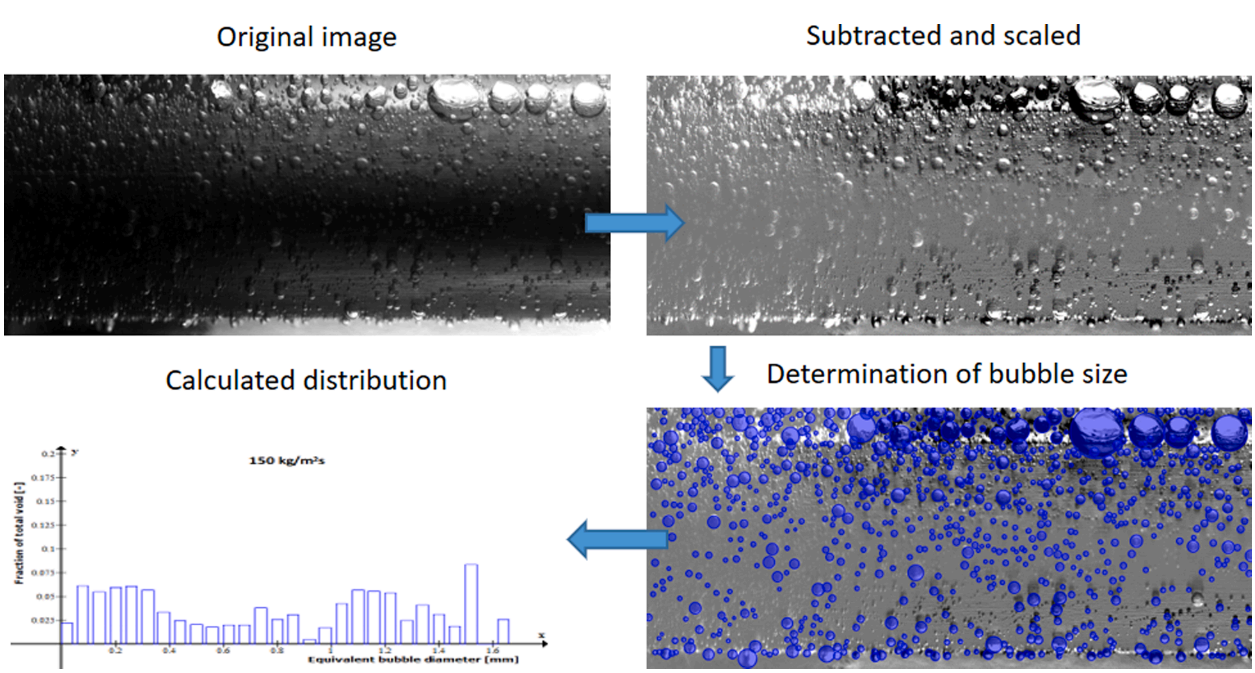

Fig. 5. Processing images and bubble size identification.

used as blank background. The acquired images were 12-bit grayscale with each pixel counts from 0 to 4096, while most of the image software and monitors can only process 8-bit brightness (0–255). To acquire the highest possible contrast, each image was scaled to 8-bit, according to its brightness histogram. For each image with subtracted background, the mean brightness and standard deviation σ were calculated and the range was determined as *mean brightness* $\pm\ \sigma$. Pixels, brighter or darker than those boundary values, were labelled correspondingly as completely black or white. While this method proved successful for improvement of contrast, subtraction resulted in a non-uniform (both black and white) bubble boundary for larger bubbles (Fig. 5, upper right).

Despite the extensive image pre-processing, the images proved to be too distorted and noised for automated bubble recognition as several different edge-detection and circle-fitting algorithms could not distinguish between bubbles, reflections and shadows caused by uneven lightning and overlapping bubbles. Bubble identification was therefore performed manually (Fig. 5, lower right). For this task, we developed a simple graphical user interface for marking the bubbles in each frame, where each bubble was fitted either with a circle or an ellipse. The resolution of this method is limited to 1 px, so all calculations were done in a pixel scale. Pixels were later transformed to dimensions in millimetres by linearly scaling the known diameter of the copper tube (1 mm $\approx$ 37 px, varied by each run). Optical distortions were also considered (see Section 3.2.1).

To present circular and elliptical bubbles in the same distribution, an equivalent radius of the circle was calculated for each bubble based on its volume. As shown schematically in Fig. 6, the bubble can be observed from one perspective only, hence the third dimension of the bubble is unknown. As the best possible approximation, all bubbles were assumed to have either spherical, spheroid (rotational ellipsoid) or general three-axial ellipsoid shape with volumes according to the Eqs. (2)–(4). Zeitoun and Shoukri [15] used similar approach.

$$V_1 = \frac{4}{3}\pi r^3 \tag{2}$$

$$V_2 = \frac{4}{3} r_a r_b^2,\ r_a > r_b, \tag{3}$$

$$V_3 = \frac{4}{3} r_a r_b \frac{1}{2} h_a,\ r_a > r_b, \tag{4}$$

For circular bubbles with $r < 0.5h_a$, a spherical shape with volume V_1 was assumed. For similarly sized elliptical bubbles, a larger length axis was used as rotational axis of resulting spheroid with volume V_2. If one of the axes exceeded half annulus width, the third axis was set to $0.5h_a$, forming a three-axial ellipsoid (following Eq. (4)). This method maintains the correct bubble dimensions from the camera field of view, while ensuring that all bubbles fit into the annular gap. Resulting volume was than transformed back to the radius of the sphere with equivalent volume. Our definition of equivalent bubble radius is therefore equal to one half of the mean Sauter diameter based on the bubble volume, $d_S = (6V/\pi)^{1/3}$.

Due to the limited depth of focus on the camera, only the largest and medium sized bubbles were clearly visible, while the smallest bubbles were blurred and difficult to detect. As there are possibly many nucleation sites on the surface, many small bubbles ($r < 3$ px) could be overlooked during the image processing. However, although the number of small bubbles can be high, their contribution to the total void volume is negligible. The fraction of void volume distributed across different bubble sizes is better representation of the impact of different bubbles on the flow regime. In this way, the emphasis is given to bubbles that have a meaningful contribution to the total void volume. The distributions of void volume across different bubble sizes are denoted as “bubble size distributions” and are presented in chapter 4.1.

3.2.1. Optical distortions

Optical distortions were calculated and considered in two steps:

1. Due to observation of boiling in cylindrical geometry, the outer glass tube acts as a cylindrical magnification lens, stretching the image in vertical direction, while maintaining the correct dimensions in the other. From known refractive indices of glass and refrigerant (1.255 at 300 K [31]), a constant magnification factor of $m = 1.25$ was determined. As the stretching occurs only in one direction, circular (spherical) bubbles should appear elliptical with one axis stretched. For such bubble, we can calculate the volume as a rotational ellipsoid (Eq. (3)) with axes $a = r$ and $b = r\,m$, resulting in a volume of $V = \frac{4}{3}\pi a^2 b = \pi r^2 m$ and showing that all volumes are multiplied with the same factor. Constant distortion factor has no effect on the bubble size distributions (Fig. 10, Fig. 11) but does affect the total void detected. During the actual bubble fitting procedure, most of the bubbles were actually fitted with circles. Upon close inspection some elongations were observed, ranging from 1.15 to 1.2. Elongation factor m was not included in the final calculation and is considered a systematic error of the bubble fitting procedure.

2. Due light refractions at the edges of glass tube, elongation factor is not constant for all bubbles. Light ray tracing from camera to constant-sized bubbles in different position of the annulus was performed and differences in bubble viewing angles were calculated. Almost no elongation was found at the centreline and most of the test section, but

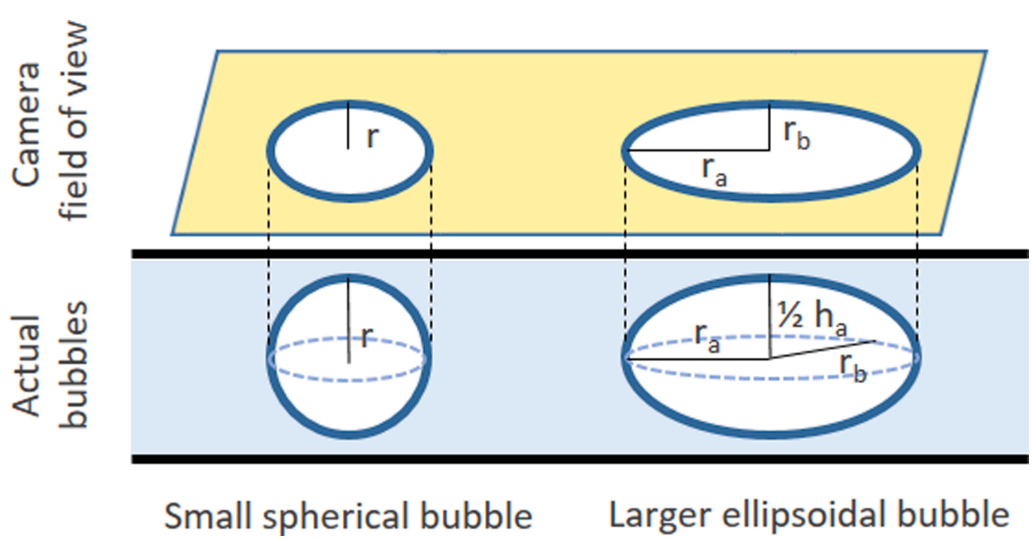

Fig. 6. Determination of bubble sizes for smaller and larger bubbles.

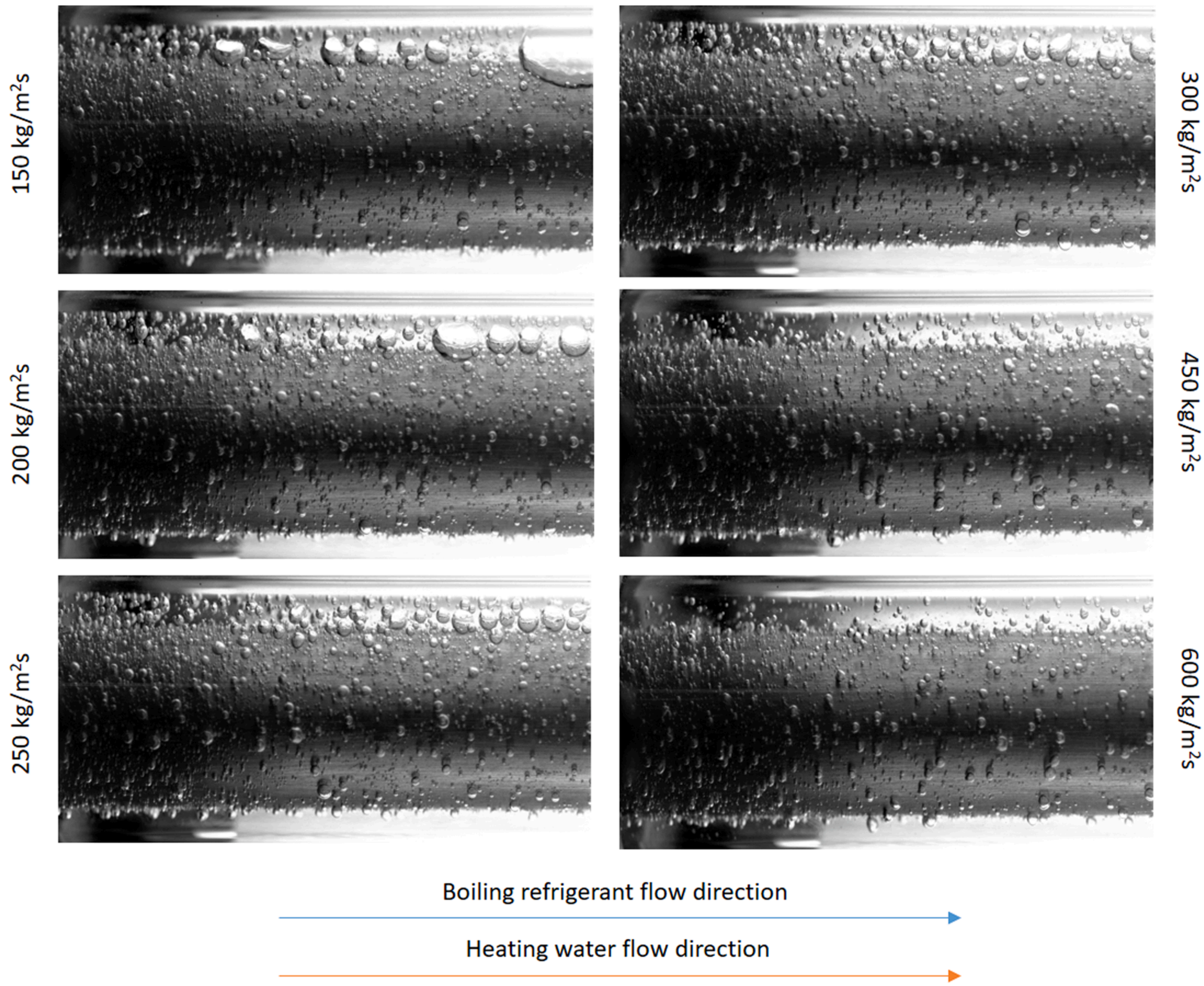

Fig. 7. Recordings of flow boiling of R245fa at different mass fluxes.

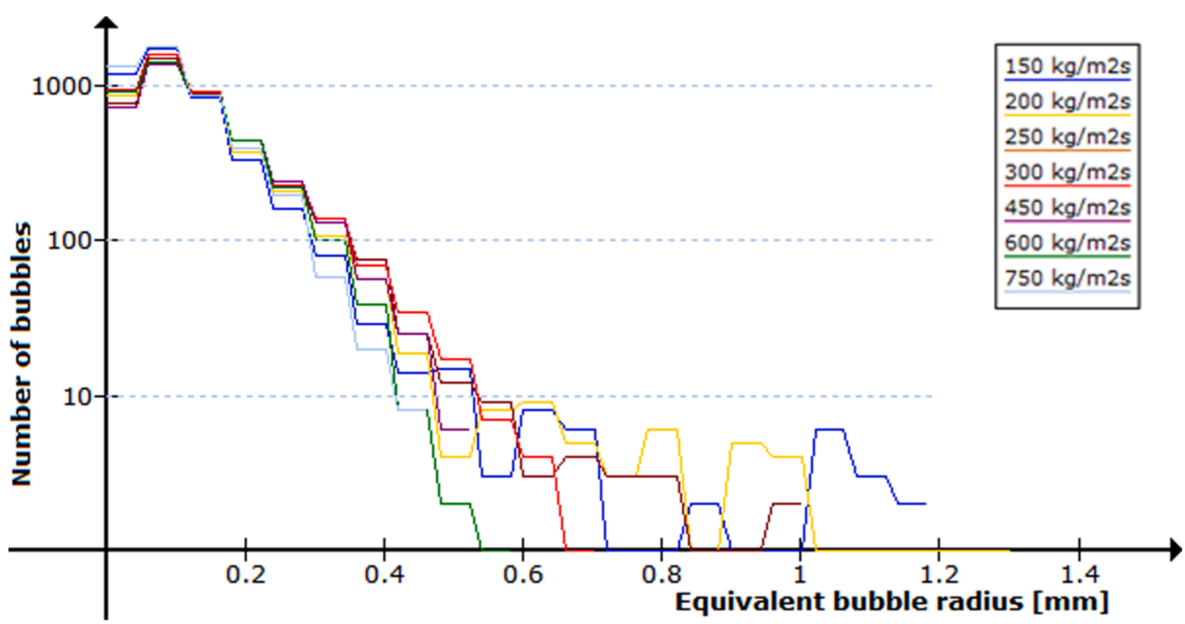

Fig. 8. Number of bubbles per bubble size at different refrigerant mass fluxes.

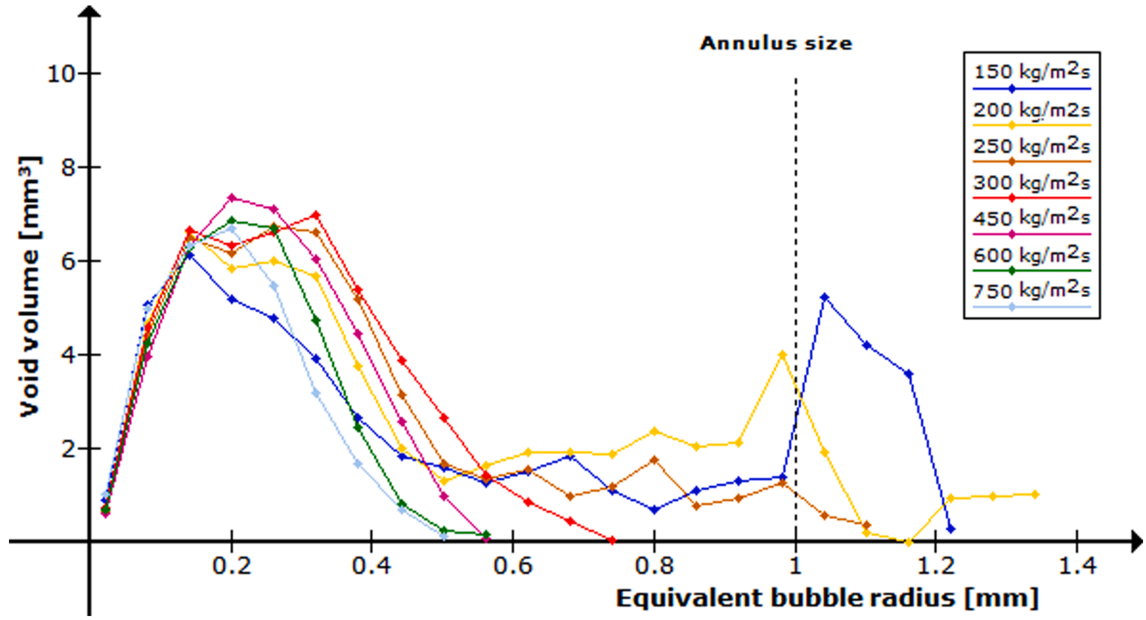

Fig. 9. Void volume distributions per bubble size at different mass fluxes.

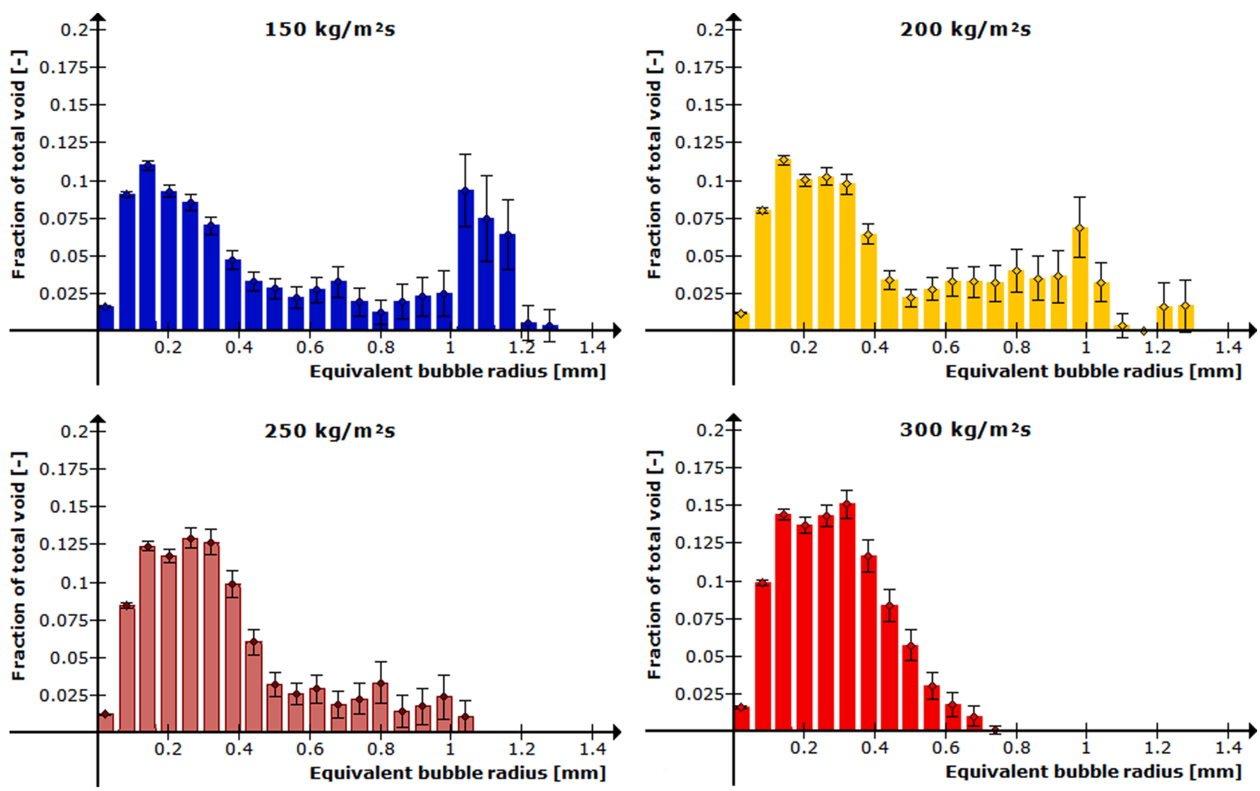

Fig. 10. Bubble size distributions at lower mass fluxes.

elongation sharply increased for bubbles the farthest from the centreline and reached a maximum of approx. 10%. Such corrections were calculated for each bubble and used in further calculations of bubble size and volume.

3.3. Uncertainty analysis of results

The uncertainty of heat flux measurements consists of temperature measurement uncertainty, thermocouple position uncertainty and the uncertainty of measured water mass flow rate. The most important contribution to the heat flux uncertainty turned out to be the uncertainty of measured temperature gradient, which was determined using the Monte Carlo method. Random noise with known uncertainty of $\pm$ 0.1 °C was added to the measured temperatures and the variation of the fitted linear function was observed. The resulting standard deviation of the slope of was used as an absolute error estimate. The obtained heat flux uncertainty is on average $\pm$ 2 kW/m^2, corresponding to the relative error of 6% to 10%, depending on the refrigerant mass flow rate.

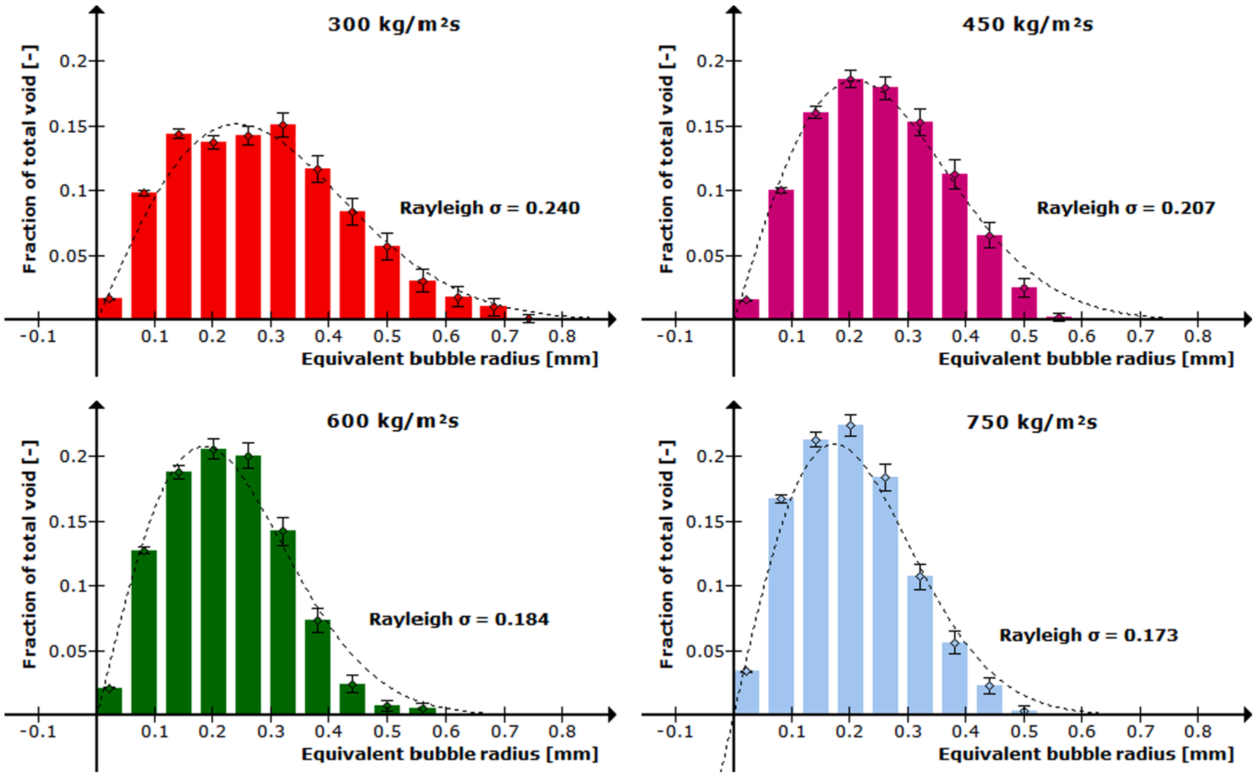

Fig. 11. Bubble size distributions at higher mass fluxes with fitted Rayleigh distributions.

For surface temperature, the thermocouples are located under the copper tube wall (see Fig. 3) and are affected by water temperature and by heat conduction. To estimate the discrepancy between the actual and measured surface temperature, numerical heat transfer simulations were performed in separate studies [2930]. The obtained temperature difference is in the range between 0.3 °C and 0.45 °C, depending on the mass flow rate and temperatures of the water and refrigerant. A conservative value of ± 1 °C was used for the uncertainty of the wall temperature measurement, as discussed in Section 2.1.

To estimate the uncertainty of fraction of void volume in bubble size distributions, one has to consider both optical distortions and the uncertainty of bubble fitting method from the images. The accuracy of length scale conversion from px to mm is around 5%, based on the known dimensions of the inner copper tube and uncertainty of ± 2 px. To estimate the error of manual bubble fitting, Monte Carlo method was used. For each experimental case, artificial uniformly distributed noise was added to all bubble radii. A noise of ± 2 px was added to each measured radius and this step was then repeated 10.000 times and, in each iteration a histogram was calculated. From all iterations, the average value of each bin and its standard deviation was determined. The average bin values are shown in Figs. 10 and 11, with standard deviations used as the error bars. The resulting variations (i.e. uncertainties) are the largest for bigger bubbles and the smallest for bubble sizes lower than 0.5 mm, where all distributions are of similar bell-curve. As this application of random noise in effect artificially increases the number of analysed bubbles, the noised distribution does not converge to the initial histogram but smooths out the sharpest peaks instead. At the same time, noise addition also reduces the effect of bin size on the histogram shape.

4. Results and discussion

All experiments were performed with a similar procedure. In horizontally oriented test section operating in co-current flow regime, the pressurizer temperature was set to 30 °C, corresponding to the saturation pressure of 1.8 bar. Heating water flow with a temperature of 60 °C and mass flow rate of 15 ± 0.3 kgh^{-1} was used to heat the refrigerant flow in the test section. Several experimental cases have been performed with different refrigerant mass flow rates, ranging from 50 kgh^{-1} to the maximum 250 kgh^{-1}, or corresponding mass flux values of 150 to 750 kg m^{-2} s^{-1} (see Table 2). Each experiment was conducted twice in order to verify the repeatability of the results. The refrigerant inlet temperature was set to 27 ± 0.5 °C.

After reaching the steady state for each experiment, stream-wise water temperature profiles were measured. For each case, all data (temperatures, pressures, flow rates) was collected in 10 s averages for a total time span of 20 min. During this period, the stability of inlet conditions was controlled. The maximum mass flow rate variation of the heating water was <2% of the average value, while the refrigerant mass flow rate fluctuations were below 0.5 %. The temperatures were constant in the range of ± 0.1 °C during the entire measurement period. At the end of the 20 min measurement, several high-speed recordings of the boiling flow pattern were performed in the time period of one minute with the frame rate of 200 frames per second. After high-speed recording, the boiling was turned off and images of the test section without boiling (filled only with the liquid phase of the refrigerant) were acquired for later background subtraction during image processing. This procedure was repeated for different experimental cases in Table 2 with the mass flow rate of heating water and refrigerant inlet temperature always remaining constant.

Despite stable saturation conditions in the pressurizer, the refrigerant inlet pressure decreases with the increasing mass flow rate due to losses in the inlet pipes. In the experiment with the lowest mass flux, the pressure was almost 0.5 bar higher than at the highest mass flux. Thus, the effective sub-cooling is not constant and in general decreases with the mass flux. The experimental data are listed in Table 2. Total void volume represents the amount of void volume integrated over all bubbles in the observed window of the test section (Fig. 3). Both the total void volume and the void fraction are given as time averaged values and multiplied by a factor of 2 to account for bubbles on the other side of the

Table 2
Experimental cases.

#	Refrigerant mass flux [kg m^{-2}s^{-1}]	Inlet pressure [bar]	Heat flux [kW/m^2]	Inlet liquid Re	T_{sub} [°C]	Total void volume [mm^3]	Void fraction [%]
1	150	2.33	20.5	1480	10.6	110	2.9
2	200	1.83	24.5	2020	5.7	116	3.1
3	250	1.78	25.0	2490	4.7	103	2.7
4	300	2.07	25.8	3000	6.6	93	2.4
5	450	1.95	28.2	4630	5.1	79	2.1
6	600	1.88	29.2	6010	4.1	60	1.6
7	750	1.85	30.5	7310	3.9	60	1.5

test section. Inlet liquid Reynolds number is based on the channel hydraulic diameter and on the refrigerant mass flux.

The boiling flow patterns are shown in Fig. 7. At the lowest mass flux (150 kg m^{-2} s^{-1}), plugs (bubbles larger than the annular gap) are periodically formed. Due to the buoyancy effect, smaller vapour bubbles generated at the bottom of the copper tube detach, slide and rise towards the upper part of the annulus where they merge with the bubbles generating on the top of the tube to form larger bubbles and vapour plugs. At a slightly higher mass flux (200 kg m^{-2} s^{-1}) the large bubbles are still being formed on the top, but the merged bubbles are smaller and very large vapour plugs can no longer be formed. With further increase of the mass flux (450 kg m^{-2} s^{-1} and above), generated bubbles are getting smaller and the higher mass flux completely prevents the formation of larger bubbles at the top. A typical dispersed bubbly flow can be observed. It can be seen that due to the buoyancy, the bubbles generated at the bottom of the tube wall slide along the bottom wall or rise towards the top of the gap. On the contrary, the bubbles generated on the top of the tube, lift-off from the wall and travel along with the liquid flow.

In Section 4.1, we analyse the bubble size distributions at different inlet mass flow rates to describe the small-scale phenomena and flow regimes. The integral results (total void volume and heat flux) are then presented in Section 4.2, where the measured heat fluxes are compared also with available empirical correlations from the literature.

4.1. Bubble size distributions

For each case in Table 2, 8 to 10 flow images (separate video frames) were processed, totalling to 8500–9500 of analysed bubbles for each flow condition. All distributions shown in Figs. 8–11 are averaged over several flow images, representing time averaged values. To avoid counting the same bubbles in multiple frames, the analysed frames were at least 500 frames (i.e. 2 s) apart. As the refrigerant liquid velocity entering the annulus cross-section is 11 cms^{-1} for the lowest mass flux, the velocities are sufficiently high for all bubbles to flow out of camera view field (4 cm in length) and no double counting occurs. This was also confirmed by careful observation of several bubbles in the boiling videos. The analysed frames can therefore be treated as separate flow snapshots. Entire images were processed to achieve as high number of bubbles as possible. Spatial variations of distributions within the observation window (left–right, top–bottom parts of the test section) have been covered in our other work [33].

Fig. 8 shows the number of analysed bubbles distributed per bubble size, represented by equivalent bubble radius. Distributions at different mass fluxes are compared. As the number of bubbles varies strongly with the bubble size, it is shown in logarithmic scale. The highest number of bubbles occurs at the smallest bubble size. The number of large bubbles is very low, there are <10 bubbles per bin at bubble radii above 0.7 mm. The statistical uncertainty in the number of large bubbles is much higher than for the smaller bubbles, where the distributions are more reliable. The scaling factor is approximately 36–37 px per mm, varying for each frame, giving a resolution of about 0.027 mm. In order to avoid the rounding error while still providing a useful visualization, a bin width of 0.06 mm (approximately double the resolution) was adopted in the histograms to represent the corresponding bubble size.

By multiplying the number of bubbles in each bin with their equivalent volume of the sphere, a distribution of the void volume over the bubble sizes can be determined, as shown in Fig. 9. The distributions are shown for different mass fluxes. The results are again histograms, presented as line plots for easier comparison. In general, the total volume of void in the observed frame decreases with the mass flux (see the last column in Table 2). As can be observed in Fig. 9, the shape of the void volume distribution per bubble size changes with the mass flux. At lower mass fluxes (150 and 200 kg m^{-2} s^{-1}) the distributions shows two different peaks, the first at approx. r = 0.3 mm and the second for bubbles around the size of the annulus. At higher mass fluxes, only one peak is visible. All distributions have a similar shape up to about r = 0.6 mm, having a similar one-peak shape. The distribution of small bubbles (r < 0.6 mm) at the highest mass flux of 750 kg m^{-2} s^{-1} is qualitatively similar to the distribution of small bubbles at lower mass fluxes of 200 and 250 kg m^{-2} s^{-1}. On the other hand, the volume of void in larger bubbles (r > 0.8 mm) is clearly decreasing with increasing mass flux. Despite their low number and associated statistical uncertainties, it can be confirmed (based on longer-time observations of the flow videos) that only a few larger bubbles are being formed at these mass fluxes and they are less and less frequent with increasing mass flux.

With further increase of the mass flux, above 250 kg m^{-2} s^{-1}, bubbles larger than the annulus gap (r > 1 mm) are no longer formed. At mass fluxes above 450 kg m^{-2} s^{-1}, the maximum observed bubble size reduces to 0.6 mm. This indicates, that a flow regime transition occurs at the mass flux around 300 kg m^{-2} s^{-1}. This transition coincides with the liquid inlet Reynolds number of about 3000.

Derived from distributions presented in Fig. 9, the fraction of void volume per bubble size was also calculated. In Figs. 10 and 11, the distributions are normalised by total void volume and each bar on the histogram represents the fraction of the void volume for the specific bubble size. Fig. 10 shows these distributions at lower mass fluxes (from 150 to 300 kg m^{-2} s^{-1}) and Fig. 11 at higher mass fluxes (between 300 and 750 kg m^{-2} s^{-1}). As seen in the histograms, the fraction of void volume at larger bubble radii reduces with the increased mass flux, just as in the total volume histograms in Fig. 9. In general, the distributions are shifting from larger bubbles to smaller bubbles as qualitatively visible in Fig. 7. The regime transition around 300 kg m^{-2} s^{-1}, as described earlier, is again present and can be observed as a gradual shift from bimodal distribution towards pronounced Rayleigh distribution. This behaviour is similar to what Prodanovic et al. [32] described as a region of significant bubble coalescence with formation of large bubbles, also appearing at low mass fluxes.

At mass fluxes above 300 kg m^{-2} s^{-1} (see Fig. 11), measured bubble size distributions follow Rayleigh distribution. The Rayleigh distribution is a one-parameter continuous distribution for positive real numbers, defined by equation

$$f(r;\sigma) = \frac{r}{\sigma^2}\exp\left(\frac{-r^2}{2\sigma^2}\right), \tag{4}$$

with a scale parameter σ and a mean value of $\sigma\sqrt{\pi/2}$. With increasing mass flux, the distributions are getting narrower, having lower σ values. Below 300 kg m^{-2} s^{-1}, a fit of Rayleigh distribution cannot describe the actual void distribution. The case with 300 kg m^{-2} s^{-1} seems to be in the transition region, while still roughly following the Rayleigh distribution. The actual fraction of void volume in larger bubbles is somewhat higher than Rayleigh distribution, while for all higher mass flux cases, the Rayleigh distribution slightly over predicts the fraction of void volume for bubbles with larger radius. This indicates that the flow regime transition occurs at the mass flux around 300 kg m^{-2} s^{-1} (inlet Reynolds number of 3000–4600).

At the lowest mass fluxes (150 and 250 kg m^{-2} s^{-1}), shown in Fig. 10, bubble size distributions can be described as bimodal, with the two peaks, one in the small and one in the large bubble regions. At the mass flux of 150 kg m^{-2} s^{-1}, a distinctly sharp second peak appears at the bubble radius of about 1.15 mm. At a higher mass flux (250 kg m^{-2} s^{-1}), the second peak shifts towards the bubbles with lower radius (~1 mm) and reduced fraction of void volume, while the overall distribution still remains roughly bimodal. Position of the first peak remains unchanged (the maximum remains below 0.2 mm), while the distribution around the first peak shows the first outlines of the Rayleigh distribution. When the mass flux is further increased (300 kg m^{-2} s^{-1}), the bimodal distribution collapses, indicating that intermediate size bubbles (radius between 0.6 and 0.8 mm) never contain a significant amount of void. This is likely a consequence of vapour gathering at the top part of the annulus, as larger bubbles formed close to the inlet move faster than the rest and capture smaller bubbles of various sizes along the way, before the intermediate sizes could form along the test section.

4.2. Heat flux and total void volume

Heat transfer in boiling flow is often understood and modelled as a combination of two phenomena - latent heat removal through liquid evaporation on the wall, and non-boiling forced convective heat transfer [45]. The increased amount of void can alter the flow pattern and may also significantly affect the heat transfer in boiling flow that is reflected in the observed heat flux. As our test section is not electrically heated but operates as a heat exchanger, the heat flux also depends on local heat transfer coefficients on solid-water and solid-refrigerant interface. Heat flux is therefore not a directly controlled variable as commonly found in the experiments from the literature [12–19,22–28]. Instead, it can be controlled by changing the mass fluxes of the heating water or the refrigerant. In this study the mass flux of heating water is kept constant while the refrigerant mass flux was varied and represents the main controlled variable. Therefore, the dependence of measured parameters is plotted against the refrigerant mass flux.

Fig. 12 shows the dependence of heat flux on the refrigerant mass flux for all cases in Table 2 (including some additional repeated measurements). As shown, higher refrigerant mass flux always leads to higher surface heat flux. This is expected when the test section behaves as a heat exchanger. Higher mass flux increases the turbulence in the liquid phase, leading to increased single-phase convective heat transfer and to smaller, more dispersed bubbles. The transition to smaller bubbles is demonstrated in Figs. 9 to 11, showing bubble distributions. With smaller bubbles, less void is present in the channel and the liquid can also reflood the heating surface more easily.

The observed change in bubble size distributions does not appear to significantly change the heat transfer characteristics. A noticeable change in void distributions per bubble size from bimodal to Rayleigh-like distributions around 300 kg m^{-2} s^{-1} appears to result in only a moderate, gradual rise of the heat flux. The dependence of heat flux on the refrigerant mass flux can be approximated by a smooth power-law function (dashed curve), as shown in Fig. 12. A large increase in refrigerant mass flux by 5 times results in increase of the heat flux by only about 30 %.

The total void volume at varied refrigerant mass flux is presented in Fig. 13. Apart from the first two points, the total void volume is declining steadily and decreases by a factor of 2 from the lowest to the highest mass flux. The decrease in total void seems monotonous, similarly as with the heat flux, no abrupt changes in the trend are visible. The first two points do not seem to follow the same trend. This observed discrepancy is likely a consequence of measurement uncertainties in the first two points related to counting of smaller number of large bubbles, implying that bubble statistics for the lowest two cases are not significant enough to distinguish the first two points apart, while it is still clear that they have the same bimodal shape of bubble size distribution.

When comparing the heat flux curve (Fig. 12) with the total void volume curve (Fig. 13), one would intuitively expect the increase of the void volume with the increased heat flux. However, just the opposite trend can be observed. It can be assumed that this is a consequence of two opposing effects appearing in this type of heat exchanger: the effect of the refrigerant mass flux versus the effect of the increased heat flux. In the case of a fixed refrigerant mass flux, the increase in heat flux would increase the surface boiling and generate higher amount of void volume in the test section. On the contrary, the increased refrigerant mass flux tends to increase the single-phase convection heat transfer, suppress the surface boiling and thus reduce the amount of void. As we are controlling the heat flux through the variation of refrigerant mass flux, it is not

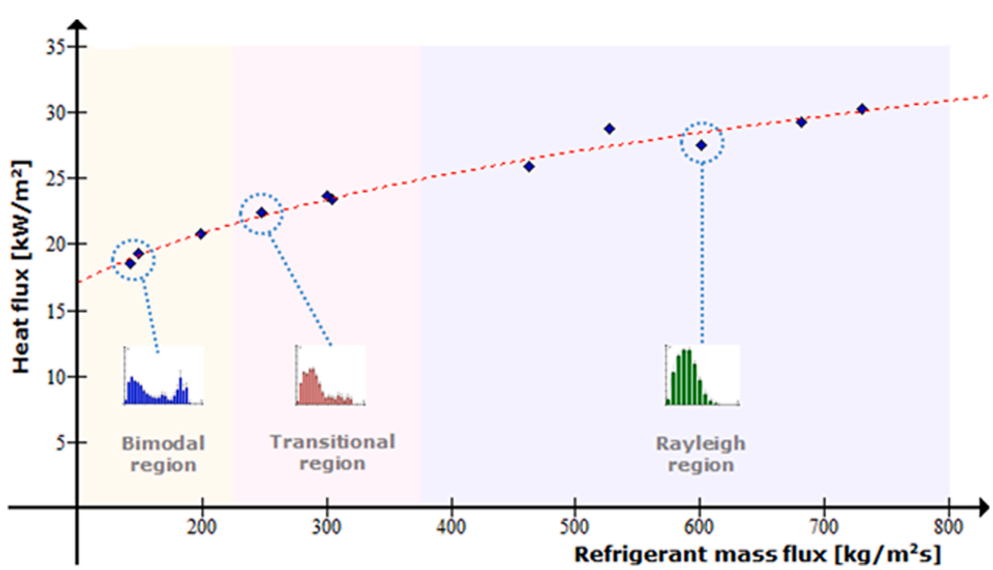

Fig. 12. Measured values of the heat flux at different refrigerant mass fluxes. Different bubble size distribution regions are shown, based on the discussion in Section 4.1.

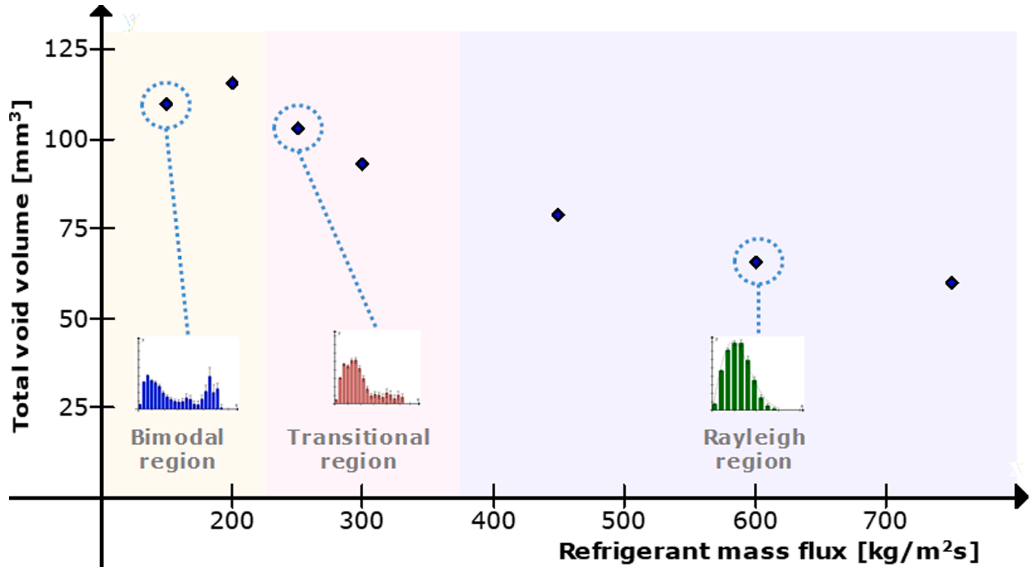

Fig. 13. Dependence of total void volume in the test section on the refrigerant mass flux. Bubble size distributions represent the three different flow regimes.

possible to isolate these two effects. As shown in Fig. 12, the increased refrigerant mass flux induces the heat flux increase. Since the total void volume (Fig. 13) in the test section is decreasing with the increased refrigerant mass flux and with the increased heat flux, it is obvious that the effect of the mass flux prevails over the heat flux effect.

To verify the heat flux results, the measurements were compared with the correlations from the literature. We have compared the results with the three widely-used general correlations for subcooled flow boiling, one developed by Shah [4] (updated in 2017) and the other two by Gungor and Winterton (1987) [5] and Liu and Winterton (1990) [6]. The comparison of experimental and predicted heat flux values is given in Fig. 14. Most of the predicted values for Shah's correlation fall between $\pm$ 30 %. Above 25 kW/m^2, the agreement with Shah's correlation is within $\pm$ 20% (both overpredicting and underpredicting experimental data). This is somewhat outside of the Shah's reported accuracy (mean absolute deviation of $\pm$ 12%), but it should be noted that Shah's fitting data did not include any measurements with refrigerant R245fa.

Correlations by Gungor-Winterton [5] and Liu-Winterton [6] both performed similarly, consistently over-predicting all measured heat fluxes by 40 – 60%. No prediction is lower than the actual experimental value. As with Shah's correlation, these two correlations didn't include any data with refrigerant R245fa. Additionally, Liu and Winterton report slightly worse agreements for large Prandtl number liquids (Pr > 6) and R245fa has a Prandtl number of 6.1. Despite overprediction of experimental data, both correlations correctly predict the trends. From the three considered correlations, Shah's correlation gives the best agreement.

5. Conclusions

Subcooled boiling of refrigerant R245fa was studied in a uniquely designed water-heated horizontal annular test section with the inner diameter of 12 mm and the annular gap of 2 mm. Detailed bubble size distributions were determined from high-speed recordings at various refrigerant mass fluxes, covering the inlet flow Reynolds numbers between 1500 and 7300.

We have demonstrated that in such horizontally positioned test section bubble size distributions shift from bimodal (two main peaks) to single peak Rayleigh distributions with increasing mass flux. Such shifting, also quantified by bubble size distributions, is to our knowledge new in the literature. Despite observing two distinct boiling flow regimes, no abrupt changes in the heat flux was observed. With the

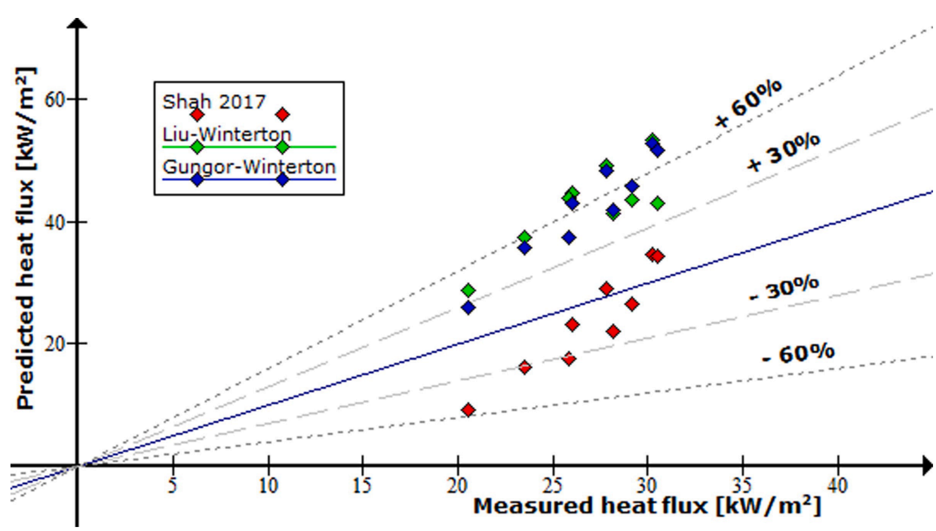

Fig. 14. Comparison of measured heat fluxes with empirical correlations.

increase of mass flux by a factor of 5, the heat flux only increased moderately by approx. 30%.

Further, it was found that in a temperature-controlled test section that operates as a heat exchanger with a variable mass flux of a working fluid (refrigerant), the two competing effects are present. The effects of the refrigerant mass flux and heat flux inherently occur together and affect the amount of total void in the observed part of the test section. The results show that the total void volume is declining steadily with the increased refrigerant mass flux, which demonstrates that the mass flux effect appears to be the main influencing mechanism and prevails over the heat flux effect. These results therefore represent a behaviour that would be expected in a realistic heat exchanger with fixed temperature and mass flux of the heating fluid in the inner pipe and changing the mass flux of the working fluid in the annulus.

CRediT authorship contribution statement

Boštjan Zajec: Investigation, Methodology, Software, Visualization, Writing – original draft, Writing – review & editing. **Leon Cizelj:** Supervision, Writing – review & editing. **Boštjan Končar:** Conceptualization, Supervision, Writing – review & editing.

Declaration of Competing Interest

The authors declare that they have no known competing financial interests or personal relationships that could have appeared to influence the work reported in this paper.

Acknowledgments

The authors gratefully acknowledge dr. M. Matkovič for his contribution in design and building of the experimental apparatus for flow boiling studies in annular geometry. The authors also gratefully acknowledge the financial support provided by the Slovenian Research Agency through the grants P2-0026, L2-9210 and L2-1827.

References

[1] S. Mancin, A. Diani, L. Rossetto, Experimental Measurements of R134a Flow Boiling Inside a 3.4-mm ID Microfin Tube, Heat Transfer Eng. 36 (14-15) (2015) 1218–1229.
[2] Y. Madhour, J. Olivier, E. Costa-Patry, S. Paredes, B. Michel, J.R. Thome, Flow Boiling of R134a in a Multi-Microchannel Heat Sink With Hotspot Heaters for Energy-Efficient Microelectronic CPU Cooling Applications, IEEE Trans. Compon. Packag. Manuf. Technol. 1 (6) (2011) 873–883.
[3] B. Končar, E. Krepper, CFD simulation of convective flow boiling of refrigerant in a vertical annulus, Nucl. Eng. Des. 238 (3) (2008) 693–706, https://doi.org/10.1016/j.nucengdes.2007.02.035.
[4] M.M. Shah, New correlation for heat transfer during subcooled boiling in plain channels and annuli, Int. J. Therm. Sci. 112 (2017) 358–370, https://doi.org/10.1016/j.ijthermalsci.2016.10.016.
[5] K.E. Gungor, R.H.S. Winterton, A general correlation for flow boiling in tubes and annuli, Int. J. Heat Mass Transf. 29 (3) (1986) 351–358.
[6] Z. Liu, R.H.S. Winterton, A general correlation for saturated and subcooled flow boiling in tubes and annuli, based on a nucleate pool boiling equation, Int. J. Heat Mass Transf. 34 (11) (1991) 2759–2766, https://doi.org/10.1016/0017-9310(91)90234-6.
[7] S. Sandler, B. Zajaczkowski, Z. Krolicki, Review on flow boiling of refrigerants R236fa and R245fa in mini and micro channels, Int. J. Heat and Mass Transf. 126 (Part A) (2018) 591–617, https://doi.org/10.1016/j.ijheatmasstransfer.2018.05.048.
[8] C.R. Kharangate, I. Mudawar, Review of computational studies on boiling and condensation, Int. J. Heat and Mass Transf. 108 (Part A) (2017) 1164–1196, https://doi.org/10.1016/j.ijheatmasstransfer.2016.12.065.
[9] Y. Sato, B. Niceno, Pool boiling simulation using an interface tracking method: From nucleate boiling to film boiling regime through critical heat flux, Int. J. Heat Mass Transf. 125 (2018) 876–890, https://doi.org/10.1016/j.ijheatmasstransfer.2018.04.131.
[10] J. Bhati, S. Paruya, J. Naik L, Numerical simulation of bubble dynamics in subcooled flow boiling in a channel, Nucl. Eng. Design, 371, 2021, ISSN 0029-5493, 10.1016/j.nucengdes.2020.110945.
[11] S. Raj, M. Pathak, M.K. Khan, An improved mechanistic model for predicting bubble characteristic size in subcooled flow boiling, Int. J. Heat Mass Transf. 149 (2020), https://doi.org/10.1016/j.ijheatmasstransfer.2019.119188.
[12] K. Kaiho, T. Okawa, K. Enoki, Measurement of the maximum bubble size distribution in water subcooled flow boiling at low pressure, Int. J. Heat and Mass Transf. 108 Part B (2017) 2365–2380, https://doi.org/10.1016/j.ijheatmasstransfer.2017.01.027.
[13] R. Sugrue, J. Buongiorno, T. McKrell, An experimental study of bubble departure diameter in subcooled flow boiling including the effects of orientation angle, subcooling, mass flux, heat flux, and pressure, Nucl. Eng. Des. 279 (2014) 182–188, https://doi.org/10.1016/j.nucengdes.2014.08.009.
[14] R. Sugrue, J. Buongiorno, A modified force-balance model for prediction of bubble departure diameter in subcooled flow boiling, Nucl. Eng. Design, 305, 2016, Pages 717-722, ISSN 0029-5493, 10.1016/j.nucengdes.2016.04.017.
[15] O. Zeitoun, M. Shoukri, Bubble Behavior and Mean Diameter in Subcooled Flow Boiling, J. Heat Transfer 118 (1996).
[16] I. Chu, S. Lee, Y.J. Youn, J.K. Park, H.S. Choi, D. Euh, C. Song, Experimental evaluation of local bubble parameters of subcooled boiling flow in a pressurized vertical annulus channel, Nucl. Eng. Des. 312 (2017) 172–183, https://doi.org/10.1016/j.nucengdes.2016.06.027.
[17] J.L. Bottini, L. Zhu, Z.J. Ooi, T.Z., C.S. Brooks, Experimental study of boiling flow in a vertical heated annulus with local two-phase measurements and visualization, Int. J. Heat and Mass Transf., 155, 2020, 10.1016/j.ijheatmasstransfer.2020.119712.
[18] A. Yadav, S. Roy, Axial and radial void fraction measurements in convective boiling flows, Chem. Eng. Sci. 157 (2017) 127–137, https://doi.org/10.1016/j.ces.2016.04.038.
[19] T.H. Lee, G.C. Park, D.J. Lee, Local flow characteristics of subcooled boiling flow of water in a vertical concentric annulus, Int. J. Multiph. Flow 28 (2020) 1351–1368.
[20] L. Zhu, Z.J. Ooi, J.L. Bottini, C.S. Brooks, J. Shan, Bubble diameter distribution and intergroup mass transfer coefficient in flows with phase change, Int. J. Heat Mass Transf. 163 (2020), https://doi.org/10.1016/j.ijheatmasstransfer.2020.120456.
[21] K. Kaiho, T. Okawa, K. Enoki, Measurement of the maximum bubble size distribution in water subcooled flow boiling at low pressure, Int. J. Heat Mass Transf. 108 (2017) 2365–2380, https://doi.org/10.1016/j.ijheatmasstransfer.2017.01.027.
[22] M. Conde-Fontenla, C. Paz, M. Concheiro, G. Ribatski, On the width and mean value of bubble size distributions under subcooled flow boiling, Exp. Therm Fluid Sci. 124 (2021), https://doi.org/10.1016/j.expthermflusci.2021.110368.
[23] R.A. Grau, K. Heiskanen, Bubble size distribution in laboratory scale flotation cells, Miner. Eng. 18 (2005) 1164–1172, https://doi.org/10.1016/j.mineng.2005.06.011.
[24] S. Nukiyama, Y. Tanasawa, An Experiment on the Atomization of Liquid: 3rd Report, On the Distribution of the Size of Droplets, Trans. Japan Soc. Mech. Eng. 5 (1939) 131–135.
[25] P. Rosin, E. Rammler, Laws governing the fineness of powdered coal, J. Institute of Fuel 7 (1933) 29–36.
[26] P. Ugandhar, A. Rajvanshi, A and D., Sarit, Investigation of Bubble Behavior in Subcooled Flow Boiling of Water in a Horizontal Annulus Using High-Speed Flow Visualization, J. Heat Transf. 34, 2017, pp. 1-15. 10.1080/01457632.2012.746544.
[27] P. Ugandhar, A. Rajvanshi, Parametric effect of pressure on bubble size distribution in subcooled flow boiling of water in a horizontal annulus, Exp. Therm Fluid Sci. 37 (2012) 164–170.
[28] M. Matkovič, L. Cizelj, I. Kljenak, B. Končar, B. Mikuž, A. Sušnik, I. Tiselj, B. Zajec, Building a Unique Test Section for Local Critical Heat Flux Studies in Light Water Reactor – Like Accident Conditions, in Proceedings of the 13th International Conference on Heat Transfer, Fluid Mechanics and Thermodynamics (HEFAT), Portorož, Slovenia, 2017.
[29] A. Kumar Basavaraj, B. Zajec, M. Matkovič, Accurate measurements of the Local Heat Transfer coefficients along the dedicated test section, in Proceedings of NENE 2018, 27th International Conference Nuclear Energy for New Europe, Portorož, Slovenia, 2018.
[30] A. Kumar Basavaraj, B. Mikuž, M. Matkovič, "Flow and Heat Transfer CFD Analysis in the Section of THELMA for Wall Surface Temperature Determination" in Proceedings of NENE 2019, 28th International Conference Nuclear Energy for New Europe, Portorož, Slovenia, 2019.
[31] J.W. Schmidt, E. Carriuo-Nava, M.R. Moldover, Partially halogenated hydrocarbons CHFC1-CF 3, CF3-CH 3, CFa-CHF-CHF 2, CF3-CH 2-CF3, CHF2-CF2-CH 2 F, CF3-CH2-CHF 2, CF3-O-CHF2: critical temperature, refractive indices, surface tension and estimates of liquid, vapour and critical densities, Fluid Phase Equilib. 122 (1996) 187–206.
[32] V. Prodanovic, D. Fraser, M. Salcudean, Bubble behavior in subcooled flow boiling of water at low pressures and low flow rates, Int. J. Multiph. Flow 28 (2002) 1–19, https://doi.org/10.1016/S0301-9322(01)00058-1.
[33] B. Zajec, B. Končar, L. Cizelj, "Visualization and Void Distribution Analysis in Flow Boiling of R245fa in Horizontal Annulus," in Proceedings of the 15th International Conference on Heat Transfer, Fluid Mechanics and Thermodynamics (HEFAT), Virtual conference, 25-28 July, 2021.